Engineered Science
DOI : https://dx.doi.org/10.30919/es931

Influence of Nonglide Stress on The Structure and Mobility of Pyramidal-I and -II $\langle c + a \rangle$ Edge Dislocations in Magnesium

Sunday Temitope Oyinbo[1, 4,#] Ryosuke Matsumoto,[2,#,*] Daisuke Matsunaka[3,#] and Tien-Chien Jen[4,#]

Abstract

Herein, molecular dynamics simulations were performed to investigate the structure and slip behavior of $\langle c + a \rangle$ edge dislocations on the pyramidal-I (Pyr-I) plane in magnesium (Mg), which were compared to those on the pyramidal-II (Pyr-II) plane. $\langle c + a \rangle$ dislocations on pyramidal planes are metastable and transition into sessile, typically sessile $\langle c \rangle$ and glissile $\langle a \rangle$ basal dislocations (basal-dissociated $\langle c \rangle$ + basal $\langle a \rangle$), or a dissociated $\langle c + a \rangle$ dislocation along the basal plane (basal-dissociated $\langle c + a \rangle$ and its derivative structure). This transition occurs at temperatures of >100 and >400 K for Pyr-I and -II $\langle c + a \rangle$ edge dislocations, respectively, in the absence of shear deformation along the slip direction, except under large non-glide stresses. The critical resolved shear stress (CRSS) of the slip plane where Pyr-I $\langle c + a \rangle$ edge dislocations glide at 10 K increases with increasing compressive or tensile strains normal to the slip plane and exhibits a minimum value of ~486 MPa. Similarly, the CRSS for Pyr-II $\langle c + a \rangle$ edge dislocations decreases with increasing compressive strains normal to the slip plane and exhibits a maximum value of ~149 MPa at 10 K. Our findings provide insights into the design of ductile Mg alloys.

Keywords: Magnesium; Pyramidal edge dislocation; Dislocation mobility; Molecular dynamics; Nonglide stress.
Received: 02 Jun 2023; Revised: 20 July 2023; Accepted: 24 July 2023.
Article type: Research article.

1. Introduction

The lattice structure of magnesium (Mg) (*i.e.*, hexagonal closed packed (HCP)) results in poor-ductility polycrystals at room temperature (T) because the number of available independent slip systems is insufficient to allow arbitrary deformation. Enhancing the ductility of Mg often requires activating non-basal deformation modes, such as dislocation slips with a $\langle c + a \rangle$ Burgers vector, to enable deformation along the c axis.[1–4]

Pyramidal $\langle c + a \rangle$ dislocation slips in Mg have recently received considerable attention. However, whether these dislocations are active on the pyramidal-I (Pyr-I) and/or pyramidal-II (Pyr-II) planes and whether edge and/or screw dislocations contribute to deformation remain a subject of active debate. A slip trace analysis conducted as part of an experimental study on c-axis compression has shown that slip traces strongly favor Pyr-II $\langle c + a \rangle$ dislocation slips.[5,6] Thus, most simulations of crystal plasticity and discrete dislocation dynamics include Pyr-II $\langle c + a \rangle$ dislocations.[7–9] The Pyr-II $\langle c + a \rangle$ dislocation is metastable and undergoes a transition, as shown by recent molecular dynamics (MD) simulations.[10,11] Thermal activation processes create sessile dislocations that are difficult to contribute to plastic strain and present formidable obstacles to subsequent slips.[12,13] The peculiar structure of a dislocation aligned along the basal plane that was discovered using MD is in agreement with previous[14,15] and very recent[16,17] transmission electron microscopy (TEM) observations that show a high density of $\langle c + a \rangle$ edge dislocations predominantly along the Pyr-II plane and basal plane intersection in the $<\bar{1}010>$ direction.

However, many MD studies conducted at very low Ts (<100 K) showed that $\langle c + a \rangle$ screw dislocations glide primarily on Pyr-I planes after being nucleated from cavities or free surfaces.[14,18] This behavior was observed even at extremely low Ts. To resolve the apparent discrepancy between the aforementioned two sets of data, Fan and El-Awady[19] reanalyzed the experimentally observed slip traces

[1] *Nagamori Institute of Actuators, Faculty of Engineering, Kyoto University of Advanced Science, 18, Yamanouchi-Gotandacho, Ukyo-ward, Kyoto 615-8577 Japan.*
[2] *Department of Mechanical and Electrical Systems Engineering, Faculty of Engineering, Kyoto University of Advanced Science, 18, Yamanouchi-Gotandacho, Ukyo-word, Kyoto 615-8577 Japan.*
[3] *Department of Mechanical Systems Engineering, Shinshu University, 4-17-1 Wakasato, Nagano 380-8553 Japan.*
[4] *Department of Mechanical Engineering Science, University of Johannesburg, 2006, South Africa.*
[#] *These authors contributed equally to this work.*
**Email:* matsumoto.ryosuke@kuas.ac.jp (R. Matsumoto).

and concluded that Pyr-I slip traces were observed rather than Pyr-II ones. These findings were corroborated by an experimental study on a Mg single crystal by Xie *et al.*[20]

The activity of pyramidal dislocations is affected by many variables, including T and nonglide stress. As mentioned above, Pyr-I and -II edge dislocations have been found to transit to basal planes at high Ts,[10,11,21] consistent with TEM studies.[17] After such transitions, $\langle c + a \rangle$ dislocations become immobilized and can no longer glide along the c axis. Notably, this process is suggested to explain why Mg exhibits characteristics such as high-strain hardening, poor ductility, and early fracture. These dislocation core transitions can also be used to explain the inverse T and strain-rate dependence of the flow stress, where the flow stress increases over a specific T range and at a low strain rate. However, these transitions are only observed at high Ts, which is not consistent with experimentally observed ductility enhancement and modest strain hardening at Ts of >400 K. This inconsistency highlights the necessity for performing additional research on the behavior of $\langle c + a \rangle$ pyramidal dislocations as a function of T and nonglide stress.

Herein, MD simulations were performed to demonstrate that Pyr-I and -II $\langle c + a \rangle$ edge dislocations are metastable and undergo a transition to various sessile dislocations. We provide quantitative data showing how T and nonglide stress affect the core structure and motion of $\langle c + a \rangle$ edge dislocations introduced on the Pyr-I and -II planes.

2. Computational modeling

2.1. Simulation method and interatomic potential

We performed MD simulations using the large-scale atomic/molecular massively parallel simulator code[22] to systematically investigate the behavior of $\langle c + a \rangle$ edge dislocations on pyramidal planes. Analyses were primarily performed on Pyr-I edge dislocations and the results were compared to those for Pyr-II edge dislocations because Pyr-II edge dislocations have already been effectively analyzed using MD.[10,11] An updated version of Wu *et al.*[23] modified embedded-atom method (MEAM)–type interatomic potential developed by Ahmad *et al.*[24] was employed in this study to describe the interatomic interactions of Mg and was specially parameterized to model the dislocation plasticity and fracture behavior of Mg. Using this potential results in the prediction of dissociated $\langle c + a \rangle$ dislocation structures along the $\langle c + a \rangle$ direction when the dislocation is placed on both the Pyr-I and -II planes, which is consistent with density functional theory calculations.[25,26] Moreover, this potential has been employed in various atomistic simulations of Mg deformation and $\langle c + a \rangle$ dislocation behavior.[10,21]

2.2. Simulation details

MD analysis is performed by introducing an edge dislocation core on the Pyr-I or -II plane into the center of a perfect HCP lattice with dimensions of approximately 30.0 (x axis) × 21.8 (y axis) × 7.5 (z axis) nm^3. The y axis is normal to the pyramidal plane, while the z axis is parallel to the dislocation line, as shown in Figs. 1a and b for the Pyr-I and -II planes, respectively. Dislocations are introduced by removing atomic layers corresponding to one Burgers vector on the upper side of the slip plane, and each atom is appropriately displaced along the x axis. Two simulation models are employed herein: a model containing a Pyr-I $\langle c + a \rangle$ edge dislocation and 143,977 atoms and a model containing a Pyr-II $\langle c + a \rangle$ edge dislocation and 145,520 atoms. Different periodic boundary conditions (PBCs) are imposed on the two simulation models. For the Pyr-I model, a PBC is only applied along the x axis and traction-free conditions are applied along the other two directions. A PBC along the z axis can strongly inhibit the dislocation core transition. However, for the Pyr-II model, PBCs are applied along the x and z axes, whereas a nonperiodic condition is applied along the y axis. The atoms in the top (positive y axis) and bottom (negative y axis) five layers are confined along the x and y axes. The confined atoms are referred to as boundary atoms herein.

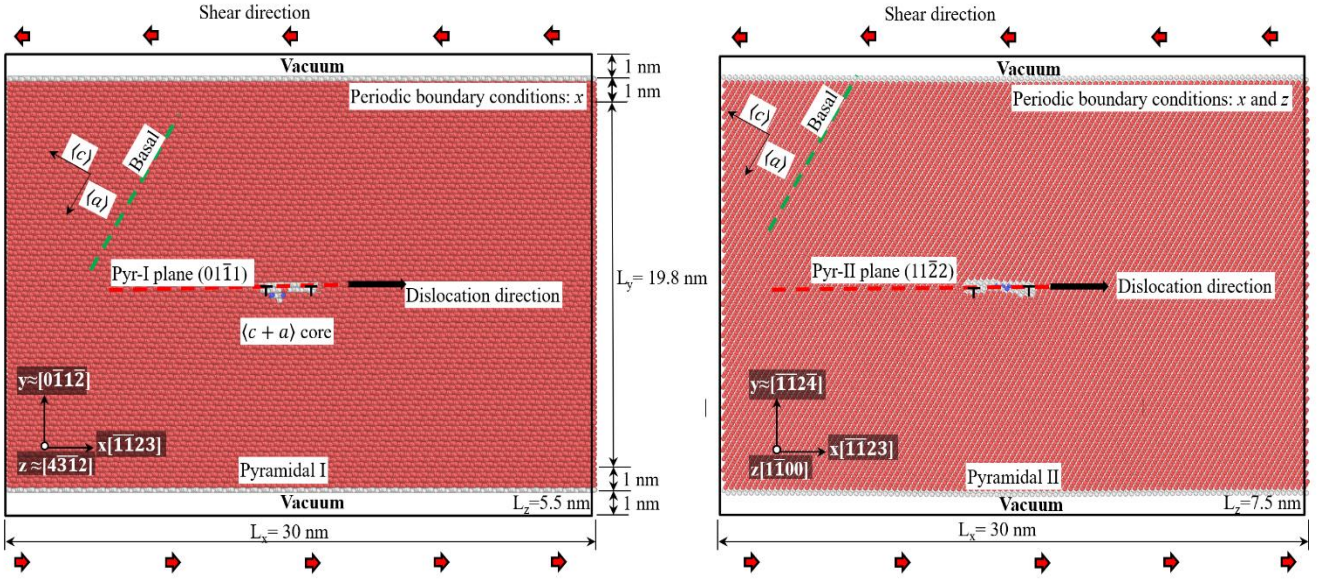

Fig. 1 Initial configuration of a single crystal of HCP Mg with a $\langle c + a \rangle$ edge dislocation core at the center on the (a) Pyr-I and (b) -II planes (a colored version of the image is available online).

After a dislocation is introduced into the system, the conjugate gradient algorithm is employed to minimize the energy with an energy tolerance of 10^{-8} while keeping fixed the boundary atoms. Simulations are performed at finite *T*s by first scaling the atomic positions from 0 K to positions suitable for finite-*T* lattice parameters. Next, the atomic velocities are randomly assigned according to a Gaussian distribution centered around the desired mean velocity at the target *T*. Simulations are performed at various *T*s (*T* = 10, 50, 100, 200, 300, 400, and 500 K). A Berendsen thermostat[27] is employed to maintain a constant *T* throughout the calculation. The simulation models are well relaxed at the specified constant *T*. A nonglide stress normal to the slip plane (normal strain ε_{yy} = −3.0%, −2.0%, −1.0%, 1.0%, 2.0%, or 3.0%) is imposed with a strain rate of 10^8 s^{-1} by moving all the atoms along the y axis. Notably, the sizes of the simulation cells are not relaxed.

Shear deformation is applied at different *T*s and normal strains to investigate the stability and mobility of the initial ⟨*c* + *a*⟩ edge dislocation on the Pyr-I and -II glide planes. To make the simulation conditions approximate experimental conditions, the dislocation is driven by imposing boundary velocity–controlled loading on the top and bottom boundary atoms in opposite directions at 1 m/s parallel to the x axis. The average dislocation speed reaches ~188 m/s if the dislocations move smoothly on the initial pyramidal planes. All the MD simulations are run using a time step of 1 fs for 2,000,000 timesteps; data are collected every 1 ps. The dislocations are analyzed using the dislocation extraction algorithm (DXA)[28] and common neighbor analysis (CNA),[29] both of which are implemented using the OVITO software.[30] In Figs. 1, 2, 3, 4, and 7, HCP, body-centered cubic, face-centered cubic, and nonstructured atoms are shown in maroon, blue, green, and white, respectively. The atoms in the dislocation core are predominantly shown in white.

3. Results and discussion

3.1 Thermally activated process for Pyr-I and -II edge dislocations under different nonglide stresses

The three columns ((i), (ii), and (iii)) of Figs. 2 and 3 show the structures of dislocation cores on the Pyr-I and -II planes, respectively, at specific instants and elevated *T*s. In the MD simulations performed to obtain these results, no shear deformation was applied along the pyramidal planes. The symbol "⊥" indicates dislocation cores with an extra plane at the upper side. The dislocations are subjected to different normal strains perpendicular to slip planes. For both slip planes, the dislocation cores undergo thermally activated processes ((ii) and (iii)).

Figure 2 illustrates the transition behavior of the Pyr-I ⟨$c + a$⟩ edge dislocation at a *T* of 300 K, which is used to accelerate any thermally activated process. The simulations are initiated using a ⟨$c + a$⟩ edge dislocation with a dissociated configuration (two partial dislocations with ⟨$c + a$⟩ components separated by a distance of ~2.7 nm) on the Pyr-I plane. The initial ⟨$c + a$⟩ dislocation is metastable and evolves into new dissociated dislocations along the basal plane. In several cases, the transition is initiated by a basal dislocation (a Shockley partial dislocation) with a near-screw orientation of ~52° to the x axis in the xy plane from one of the two partial dislocations. The Shockley partial dislocation glides a short distance, leaving behind an intrinsic basal I_2 stacking fault ($SF\ I_2$) and an edge dislocation with a 1/2⟨c⟩ component (except in Fig. 2d(i)).[4] This formation of a near-screw Shockley partial dislocation easily occurs under tension, even at 10 K, before shear deformation, as shown in Fig. 4d(i). The ⟨$c + a$⟩ dislocation then climb-dissociates onto the basal plane (producing a basal-dissociated ⟨$c + a$⟩ dislocation), resulting in the formation of an intrinsic I_1 basal stacking fault ($SF\ I_1$) and effectively making the dislocation sessile ((ii) of Figs. 2a, b, and d). The third image (iii) in Figs. 2a, b, and d indicates that except under large compression ($\varepsilon_{yy} = -3\%$, Fig. 2c), the initially introduced dislocation on the Pyr-I plane finally splits into three cores connected by two stacking faults; the near-screw Shockley partial dislocation is connected to a partial dislocation with a 1/2⟨c⟩ component by $SF\ I_2$ on the basal plane, and a partial dislocation with a ⟨$c + a$⟩ component aligned on the basal plane is connected to the ⟨c⟩ dislocation by an extrinsic stacking fault ($SF\ E$). This complete transition with climb motion occurs at a *T* of >100 K on the MD time scale. The transition is confirmed to be delayed under tension (Fig. 2d(iii)). At a large compressive strain ($\varepsilon_{yy} = -3\%$, Fig. 2c), the Pyr-I ⟨$c + a$⟩ edge dislocation transforms into a basal-dissociated ⟨$c + a$⟩ dislocation and two Shockley partial dislocations with different signs.

Figure 3 shows the transition of the Pyr-II ⟨$c + a$⟩ edge dislocation at 500 K that preferentially occurs under zero strain (Fig. 3a) and compressive strain ($\varepsilon_{yy} = -1\%$ (Fig. 3b) and −3% (Fig. 3c)) in the absence of shear deformation. The dislocation on the Pyr-II plane also dissociates into two partial dislocations separated by ~3.8 nm ((i)). Notably, intense atomic vibrations at 500 K can cause misjudgment in analyzing the structure of dislocations via CNA; thus, many white atoms (defects) appear around the dislocation core. The left cores of the two partial dislocations nucleate a Shockley partial dislocation ((ii)). The newly nucleated partial ⟨a⟩ dislocation remains close to the original nucleation site. This dislocation core has already been reported[15,26] and has been recently resolved using high-angle annular dark-field scanning TEM.[17] The third column (iii) shows the final transition state of the dislocation. The dislocation splits into ⟨c⟩ (two partial dislocations with 1/2⟨c⟩ components) and ⟨a⟩ (a pair of Shockley partial dislocations) by nucleating a trailing partial dislocation behind the leading partial dislocation (basal-dissociated ⟨c⟩ + basal ⟨a⟩). Under zero strain, both the basal-dissociated ⟨c⟩ and ⟨a⟩ dislocations remain close to each other (Fig. 3a(iii)). Under the application of a normal strain, the ⟨a⟩ dislocation glides away because of the resolved shear stress (RSS) from the applied compressive strain (Figs. 3b(iii) and c(iii)), leaving behind two 1/2⟨c⟩ partial dislocations.

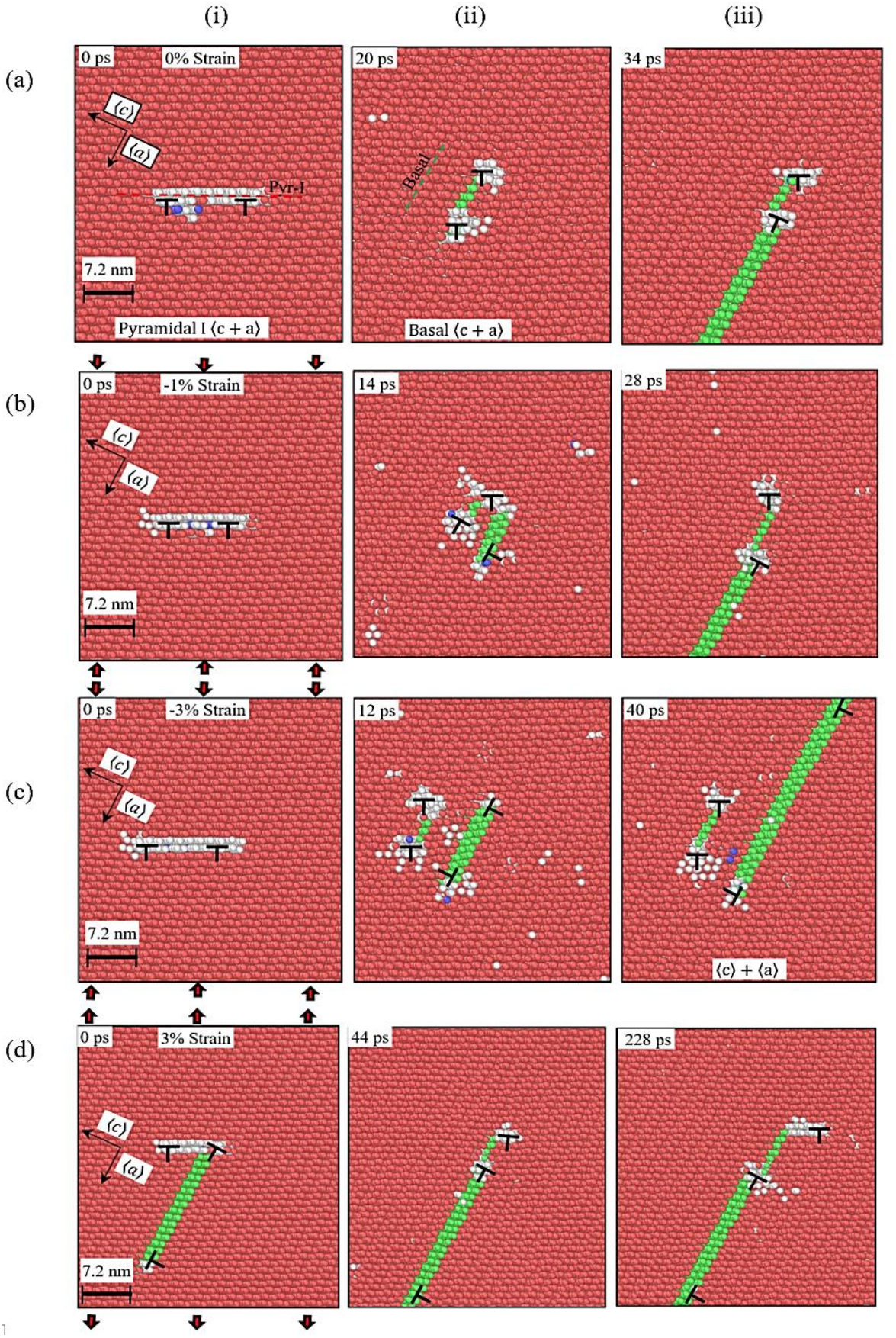

Fig. 2 Transition of the Pyr-I $\langle c + a \rangle$ edge dislocation at 300 K. MD simulations show that the $\langle c + a \rangle$ dislocation transforms into basal-dissociated products under normal strains of (a) zero, (b) −1%, (c) −3%, and (d) 3%. Columns (i), (ii), and (iii) show the dislocation structure after relaxation, a typical dislocation structure during the transition, and the dislocation structure after the transition, respectively (colored versions of the images are available online).

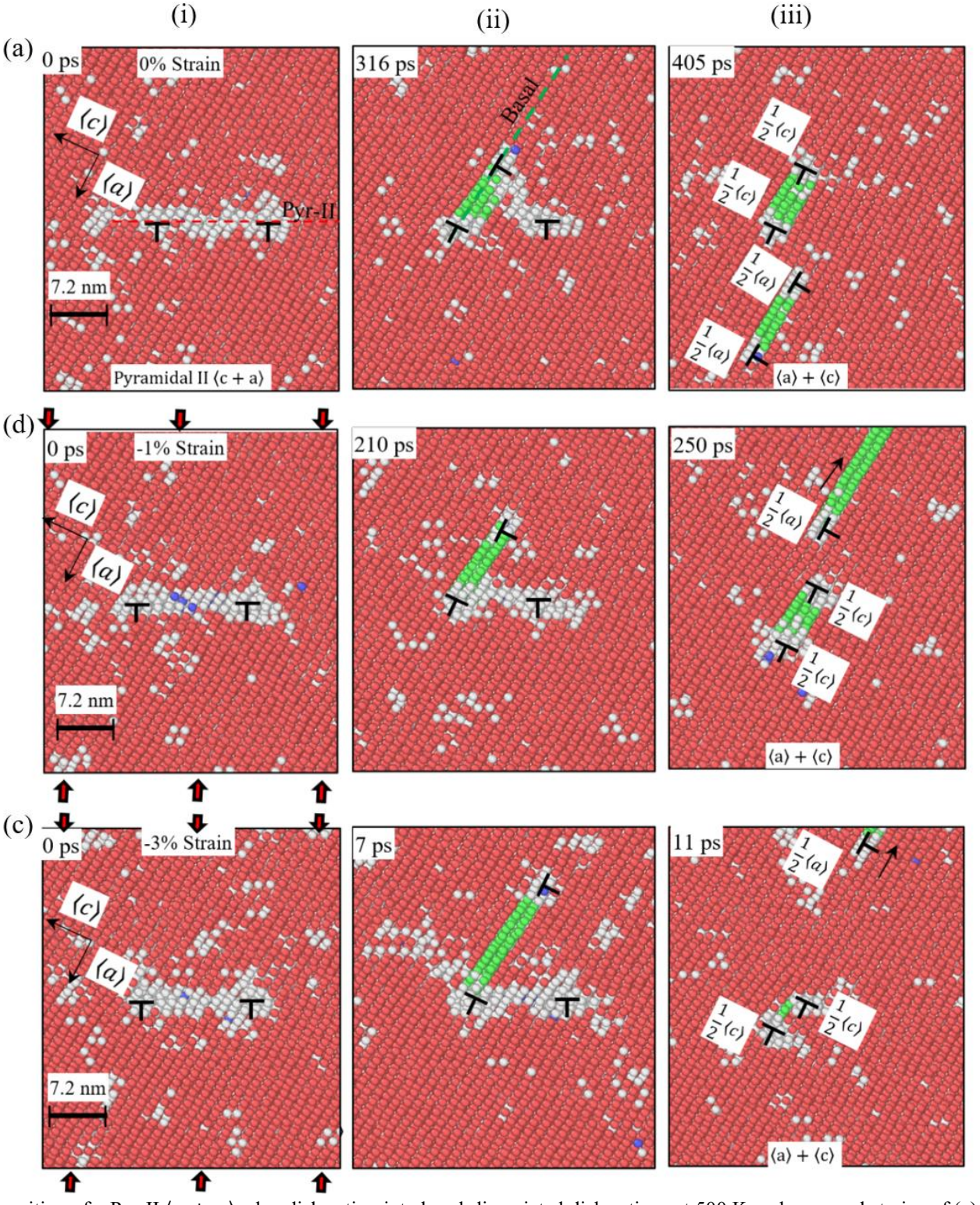

Fig. 3 Transition of a Pyr-II $\langle c + a \rangle$ edge dislocation into basal-dissociated dislocations at 500 K under normal strains of (a) zero, (b) −1%, and (c) −3%. Columns (i), (ii), and (iii) show the dislocation structure after relaxation, a typical dislocation structure during the transition, and the dislocation structure after the transition, respectively (a colored version of the image is available online).

Subsequently, one $1/2\langle c \rangle$ partial dislocation induces climb motion of the other dislocation. The dislocations align with each other along the $\langle a \rangle$ direction and connect through a basal *SF E* (a basal-dissociated $\langle c \rangle$ dislocation), in accordance with TEM observations.[15,31] The formation of the leading $\langle a \rangle$ partial dislocation and the subsequent trailing part occurs under compression or zero strain at a T of >400 K. Under tensile strain, this phenomenon does not occur until 2 ns of the simulation. Thus, the transition is enhanced by compression normal to the slip plane.

3.2 Migration behavior and CRSS of Pyr-I and -II $\langle c + a \rangle$ edge dislocations under different normal strains at a low T

Figure 4 shows the motion of the dislocation on the Pyr-I plane at 10 K under different normal strains. A complete transition of the Pyr-I dislocation is difficult, as described in Section 3.1, to occur at this T in the absence of shear deformation. However, a Shockley partial dislocation is formed from one of the partial dislocations with a Pyr-I $\langle c + a \rangle$ component. The dislocation structures under four normal strains perpendicular to the slip plane (ε_{yy} = 0%, −1%, −3%, and 3%) at the beginning of shear deformation are shown in the first column (i) of Fig. 4. The typical deformed states of the structure are shown on the right side ((ii), (iii), and (iv)) of each row of the figure.

The migration of the Pyr-I dislocation can be attributed to the "tail-cutting" behavior, except under very large compression ($\varepsilon = -3\%$ (Fig. 4c)). The second column ((ii)) in Figs. 4a and b shows the nucleation of a Shockley partial dislocation with a near-screw attribute from one of the partial dislocations on the Pyr-I plane under $\varepsilon = 0\%$ and -1%, respectively. The nucleated Shockley partial dislocation $\langle a_1 \rangle$ glides away, generating a basal $SF\ I_2$; this dissociation restricts the glide of the Pyr-I dislocation. Then, as shown in the third column (iii) in Figs. 4a and b, another Shockley partial dislocation $\langle a_2 \rangle$ with a different sign nucleated from the partial dislocation with a $\langle c \rangle$ component under a larger shear stress and the dislocation on the Pyr-I plane recovers the glissile $\langle c + a \rangle$ component. Meanwhile, the shear stress reaches a maximum, which is defined as the critical resolved shear stress (CRSS) for the Pyr-I dislocation with a "tail-cutting" motion (Fig. 5a). After formation, the two Shockley partial dislocations with different signs annihilate each other. The Pyr-I dislocation glides some distance (Figs. 4a(iv) and b(iv)), during which vacancies are generated because the two partial dislocations occur on different planes. This phenomenon occurs because the $\langle c \rangle$ dislocation shown in Figs. 4a(ii) and b(ii) can migrate slightly downward and can be recovered as a $\langle c + a \rangle$ dislocation on a different Pyr-I plane. The Pyr-I dislocation migrates some distance, forms a

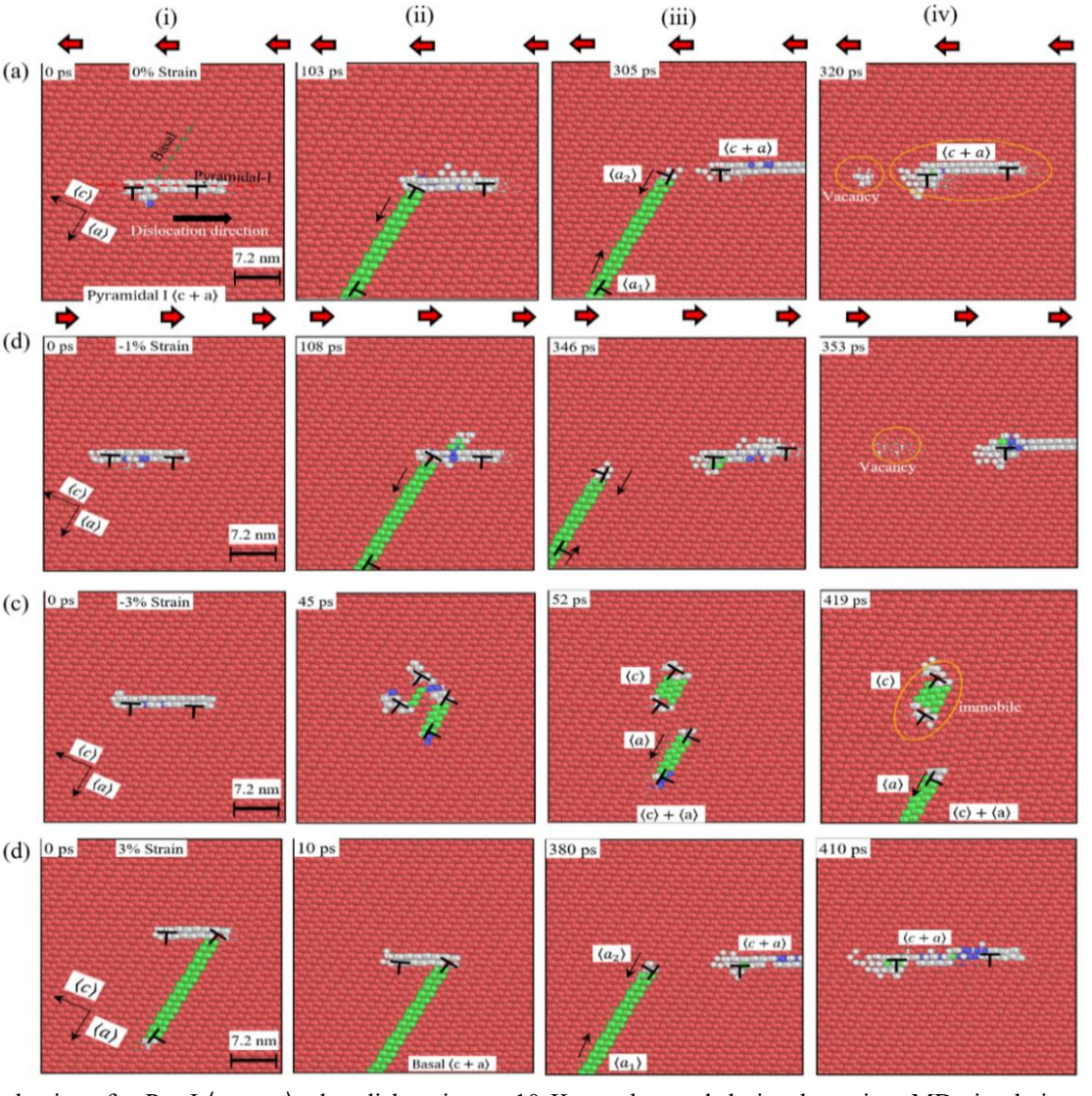

Fig. 4 Glide behavior of a Pyr-I $\langle c + a \rangle$ edge dislocation at 10 K, as observed during long-time MD simulations, under shear deformation for normal strains of (a) 0%, (b) −1%, (c) −3%, and (d) 3%. The direction of the shear deformation is shown by the arrows in (a) (a color version of the image is available online).

Shockley partial dislocation $\langle a_1 \rangle$ again, and returns to the state shown in the second column in Figs. 4a(ii) and b(ii). The leading Shockley dislocations are formed downward from the Pyr-I dislocation in most cases, as shown in Fig. 4, but are sometimes formed upward. No discernible difference is present between the leading Shockley dislocations emitted upward and downward, which exhibit the same "tail-cutting" behavior.

The dislocation motion under tension ($\varepsilon = 1\%$, 2%, and 3%) is generally similar to that described above. However, the nucleation position of the Shockley partial dislocation is different; the Shockley partial dislocation is formed from the left core of the Pyr-I dislocation under zero strain and compression but from the right core under tension (Figs. 4d(i) and d(ii)). Another difference is that the formation occurs in the absence of shear deformation under tension (Fig. 4d(i)). The left core, which has a $\langle c + a \rangle$ Burgers vector component, still has mobility and moves rightward to overtake the right core, which has a $\langle c \rangle$ component between the times shown in Figs. 4d(ii) and d(iii). Then, a process same as that of the aforementioned "tail-cutting" behavior occurs. That is, the dislocation core with a $\langle c \rangle$ component migrates slightly downward, forms a Shockley partial dislocation with a different sign, and recovers mobility along $\langle c + a \rangle$ on the Pyr-I plane while vacancies nucleate during the migration (Fig. 4d(iv)).

From a comparison between Figs. 4c(ii) and (iii), it can be seen that the Pyr-I $\langle c + a \rangle$ edge dislocation core transforms into dissociated $\langle c \rangle$ and $\langle a \rangle$ dislocations under a high compressive strain ($\varepsilon = -3\%$). Then, the shear stress causes the $\langle a \rangle$ dislocation to glide away, leaving an immobile $\langle c \rangle$ dislocation behind (Fig. 4c(iv)). We confirmed that this transition does not occur within the same simulation period at 10 K in the absence of shear deformation. However, the transition occurs at 10 K after the application of shear over the simulation time scale. This result shows that compression and shear deformation enhance decomposition into $\langle c \rangle$ and $\langle a \rangle$, making the slip difficult.

Figure 5a show the CRSSs for the Pyr-I and -II $\langle c + a \rangle$ edge dislocations as functions of the normal strain. For comparison, the time evolution of the shear stress for the Pyr-I and -II dislocations is shown in Figs. 5(b)–(e). In Fig. 5a, the red filled symbols represent the CRSS (τ_{xy}) for which the Pyr-I $\langle c + a \rangle$ edge dislocations glide on their original plane with "tail-cutting" behavior (the value corresponding to the first peak in Figs. 5b and c) and the red half-filled symbols indicate the shear stress τ_{xy} required for the nucleation of the leading Shockley partial dislocation from the $\langle c + a \rangle$ dislocation. As explained above, the $\langle a_1 \rangle$ dislocation nucleates from the $\langle c + a \rangle$ dislocation in the absence of shear deformation under tensile stress. Thus, the red half-filled symbols are only plotted at $\varepsilon_{yy} = 0\%$, -1%, and -2%. The shear stress for the Pyr-I $\langle c + a \rangle$ edge dislocation at $\varepsilon_{yy} = -3\%$ is not shown because the dislocation transforms into a sessile dislocation (Fig. 4c(iv)), resulting in catastrophic deformation at a high shear stress (~800 MPa, as shown in Fig. 5b). The blue filled symbols indicate the CRSS for easy gliding of the Pyr-II $\langle c + a \rangle$ edge dislocation at 10 K. The dislocation moves with stop-and-go motion while the structure remains on the Pyr-II plane. The CRSS for the Pyr-II $\langle c + a \rangle$ edge dislocation is also defined as the first peak value of the shear stress τ_{xy} (Figs. 5d and e). The CRSS for the Pyr-I edge dislocation increases with increasing tensile strain and exhibits a minimum value of approximately 486 MPa at $\varepsilon_{yy} = 0\%$. This behavior is caused by the nucleation of the Shockley partial dislocation, preventing the Pyr-I slip (Fig. 4d(ii)). The nucleation of the Shockley partial dislocation with the opposite sign (Fig. 4d(iii)), which causes "tail cutting," is prevented by the action of the tensile strain. Similarly, the CRSS for the Pyr-I $\langle c + a \rangle$ edge dislocations under compression also increases. This result can be explained by considering that increasing the compressive strain favors the transition of the $\langle c + a \rangle$ edge dislocation to the basal plane (Fig. 4c(iii)) and destabilizes the easy-gliding dislocation core structure. The CRSS of the Pyr-II $\langle c + a \rangle$ edge dislocation is observed to decrease with increasing compressive strain, and it exhibits a maximum value of approximately 149 MPa at 0% strain. As the initial dislocation core structure is very stable at 10 K, the dissociation or formation of Shockley partial dislocations does not affect the mobility of the $\langle c + a \rangle$ edge dislocation. This analysis cannot explain the decrease in the CRSS for the Pyr-II slip under compression, although the dislocation core structure is flat at the compression side. A previous MD simulation has also shown that Pyr-II edge dislocations have higher mobilities than Pyr-I edge dislocations at relatively low Ts.[19]

The shear direction is found to affect the motion of the Pyr-I dislocation owing to the asymmetric dislocation core structure. Changing the sign of the shear deformation results in higher CRSSs (by approximately 100 MPa) and the generation of more vacancies under all normal strain conditions. However, the migration behavior remains the same, except that the mobile $\langle c + a \rangle$ dislocation must overtake the $1/2\langle c \rangle$ partial dislocation after the formation of the Shockley partial dislocation, similar to the behavior shown in Fig. 4d. Furthermore, the Shockley partial dislocation remains near the $1/2\langle c \rangle$ partial dislocation under the opposing driving force. This behavior may prevent the nucleation of a second Shockley partial dislocation with the opposite sign, and it increases the CRSS. Shear deformation with the opposite sign is expected to prevent the nucleation of the leading Shockley partial dislocation and restrain the "tail-cutting" behavior; however, this is not observed in the MD simulation.

Figure 6 shows the CRSS for the Pyr-I and -II edge dislocations at elevated Ts as wells as the CRSS shown in Fig. 5a. The CRSS is plotted as a function of the applied normal strain at 10 and 50 K for the Pyr-I slip and at 100, 200, 300, and 400 K for the Pyr-II slip. The aforementioned Ts are below the transition T on the simulation time scale (except for the Pyr-I slip under a higher compressive strain, where the

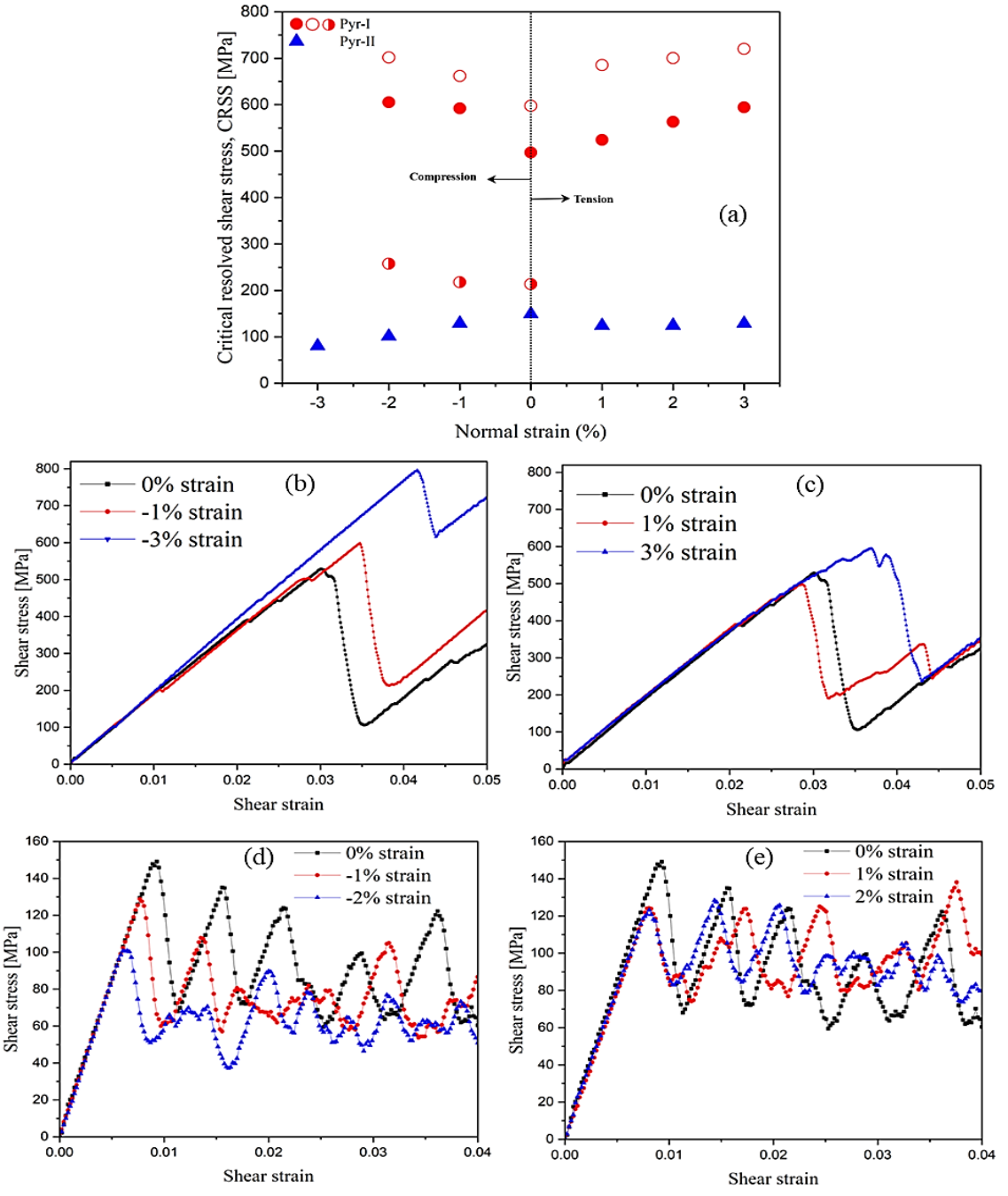

Fig. 5 (a) CRSS (the first peak value of the shear stress) as a function of the normal strain for the Pyr-I and -II $\langle c + a \rangle$ edge dislocations at 10 K. The solid symbols represent the CRSS for the Pyr-I (red circles) and -II (blue triangles) dislocations, and the half-filled symbols represent the stress at which the Pyr-I dislocation undergoes transformation or decomposition. The time evolution of the shear stress of the Pyr-I $\langle c + a \rangle$ edge dislocation under (b) compression and (c) tension. The time evolution of the shear stress of the Pyr-II $\langle c + a \rangle$ edge dislocation under (d) compression and (e) tension (colored versions of the images are available online).

transition is likely to occur). The CRSS decreases with increasing T owing to the increased thermal activation of the dislocation glides. This T dependency is normal and is observed for most materials.

3.3. Glide behavior of various dislocations at a high T

Figure 7 illustrates the glide behavior of various basal-dissociated dislocations under different normal strains ($\varepsilon_{yy} =$ 0%, −1%, −3%, and 3%) perpendicular to the Pyr-I plane under shear deformation at 300 K. The dislocation structures at the beginning of shear deformation are presented in the first column (i) of Fig. 7. At this T, as described in Section 3.1, the initial $\langle c + a \rangle$ cores rapidly evolve into new dissociated dislocations along the basal plane via a thermally activated process ((ii) of Fig. 7). All the dislocation cores are essentially sessile under the current deformation speed after the transition, which is expected considering the dissociation of these cores into nongliding structures. Hence, complex and catastrophic

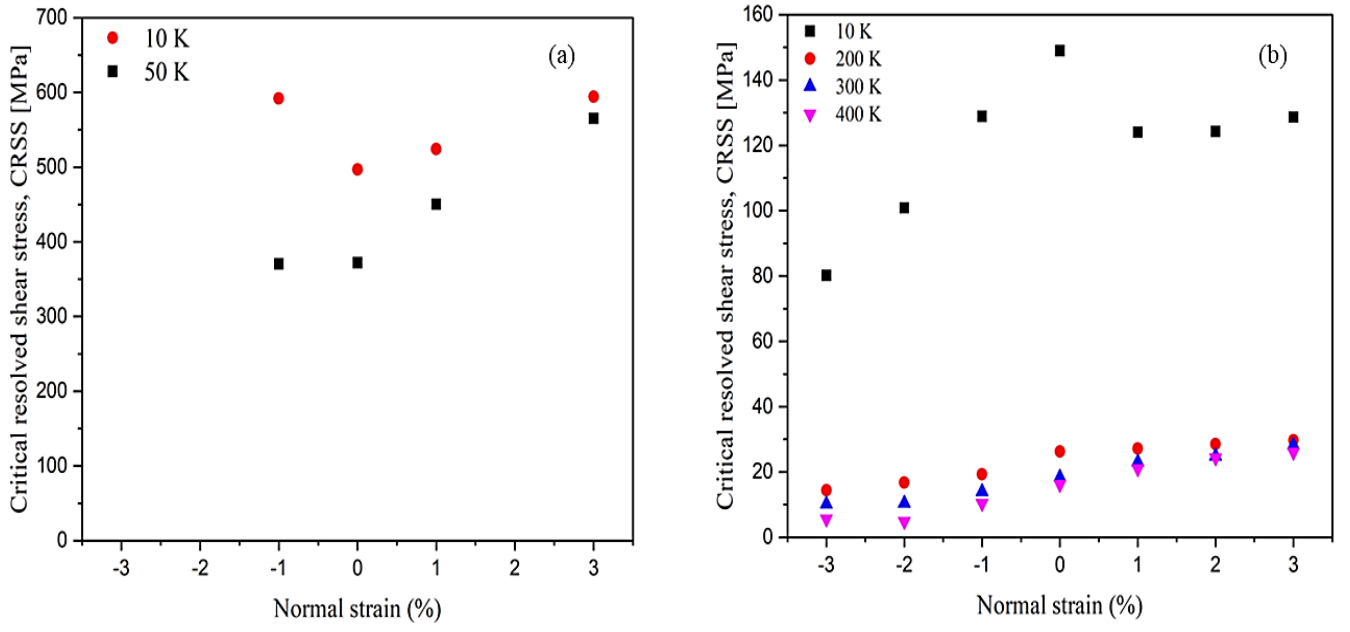

Fig. 6 CRSS as a function of the normal strain for (a) Pyr-I and (b) -II $\langle c + a \rangle$ edge dislocations at various *T*s (colored versions of the images are available online).

phenomena occur at high stress. The fourth column (iv) of Fig. 7 corresponds the instant immediately before the catastrophic phenomena occur. The shear stress τ_{xy} at each instant is shown in the figures. Figures after the instance shown in (iv) are omitted because the defect activities are difficult to explain. The phenomena are probabilistic in nature and are affected by small differences in the initial conditions and thermal effects.

In Fig. 7a, at $\varepsilon_{yy} = 0$, the Pyr-I $\langle c + a \rangle$ dislocation first transforms into the basal-dissociated $\langle c + a \rangle$ structure ((ii)). Almost no change is observed for this dislocation up to ~107 MPa (Fig. 7a(iii)), beyond which the Shockley partial dislocation is nucleated. This transition proceeds similarly to that in the absence of shear shown in Fig. 2a(ii). No further glide is observed, and the basal-dissociated $\langle c + a \rangle$ dislocation remains immobile as the shear stress increases, causing further deformation at a high shear stress of ~738 MPa (Fig. 7a(iv)).

At an applied strain $\varepsilon = -1\%$, the Pyr-I dislocation transforms into a basal-dissociated $\langle c \rangle$ + basal $\langle a \rangle$ structure (Fig. 7b(ii)) and the $\langle a \rangle$ dislocation glides away at ~348 MPa leaving behind a sessile $\langle c \rangle$ dislocation (Fig. 7b(iii)). This result shows that even under low compression, high *T* and shear deformation can enhance the decomposition of Pyr-I $\langle c + a \rangle$ dislocation into a basal-dissociated $\langle c \rangle$ + basal $\langle a \rangle$ dislocation. Subsequently, the two half-sessile $\langle c \rangle$ dislocations react with the residual dislocation at a high shear stress of ~597 MPa to form two additional partial dislocations with a $\langle c + a \rangle$ component (Fig. 7b(iv)). At an applied strain $\varepsilon = -3\%$ (Fig. 7c), the Pyr-I $\langle c + a \rangle$ edge dislocation also decomposes into two $\langle c + a \rangle$ partial dislocations and two Shockley partial dislocations with different signs (Fig. 7c(ii)), as observed for the thermally activated process in the absence of shear (Fig. 2c(ii)). The two Shockley partial dislocations exhibit opposing motion under a high shear stress of ~521 MPa and the RSS from the compressive stress (Fig. 7c(iii)), making the slip difficult.

A stress of ~256 MPa is required to induce decomposition of the basal-dissociated $\langle c + a \rangle$ dislocation under a 3% tensile strain into prismatic $\langle c \rangle$ and basal $\langle a \rangle$ dislocations (Fig. 7d(iii)). Notably, with increasing shear deformation, the $\langle c \rangle$ and $\langle a \rangle$ dislocations glide away along the prismatic and basal planes, respectively, as shown in Figs. 7d(iii) and (iv). After migrating a short distance, the dislocation with a $\langle c \rangle$ component is transformed into a sessile structure with a basal-dissociated $\langle c \rangle$ component. MD calculations show that the RSS from the tensile strain becomes quite high on the prismatic plane.

In summary, at a *T* higher than the transition *T* (100 K for the Pyr-I plane in this study), the dissociated dislocations formed from a Pyr-I edge dislocation are difficult to contribute to deformation under all normal strains perpendicular to the slip plane and under the investigated deformation speed where thermally activated dislocation motion is limited. The required stress is higher than the CRSS for the "tail-cutting" behavior shown in Fig. 6. Thus, the stress for the Pyr-I edge dislocation also exhibits an inverse *T* dependence.

4. Conclusion

Herein, MD simulations were performed to study the thermally activated process and mobility of Pyr-I $\langle c + a \rangle$ edge dislocations at different nonglide stresses and *T*s for comparing them with those corresponding to Pyr-II $\langle c + a \rangle$ edge dislocations. The Pyr-I $\langle c + a \rangle$ edge dislocation is metastable. Under nonglide and stress-dependent glide thermally activated processes, the Pyr-I $\langle c + a \rangle$ edge dislocation undergoes a transition to a sessile dislocation (*i.e.*,

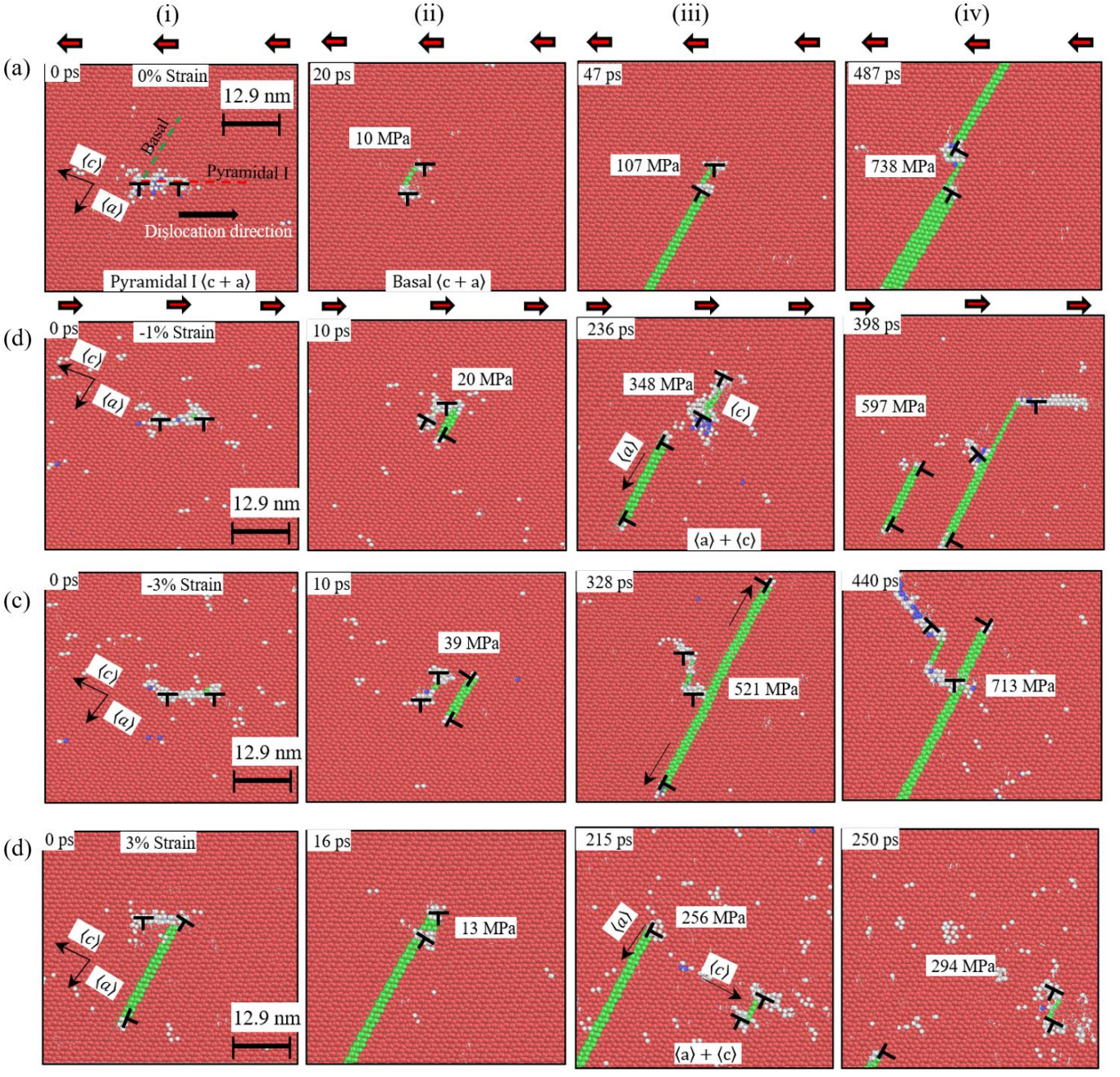

Fig. 7 Details of the dissociation of a Pyr-I $\langle c + a \rangle$ edge dislocation into basal-dissociated products and behavior at a high shear stress for the following values of normal strains perpendicular to the Pyr-I plane at 300 K: (a) 0%, (b) −1%, (c) −3%, and (d) 3%. The red arrow at the top and bottom edges of (a) indicates the direction of shear deformation (a colored version of the image is available online).

a basal-dissociated $\langle c \rangle$ + basal $\langle a \rangle$ structure or a basal-dissociated $\langle c + a \rangle$ and its derivative structure).

1. The observed transition is inherent to pure Mg and occurs at Ts of >100 and >400 K for Pyr-I and -II $\langle c + a \rangle$ edge dislocations, respectively, except under large nonglide stresses. Thus, the Pyr-I dislocation is more thermally unstable than the Pyr-II dislocation. The application of a tensile stress perpendicular to the slip plane delays the transition for both the Pyr-I and -II dislocations.

2. At a T below the transition T, the Pyr-I edge dislocation migrates with a characteristic "tail-cutting" behavior, except under large compression. However, the CRSS for this motion is considerably higher than that for the Pyr-II edge dislocation. The CRSS at which the Pyr-I $\langle c + a \rangle$ edge dislocation glides on its original plane increases with increasing compressive or tensile strains normal to the slip plane and exhibits a minimum value of ~486 MPa at 10 K. Similarly, the CRSS for the Pyr-II $\langle c + a \rangle$ edge dislocation decreases with increasing compressive strains normal to the slip plane and exhibits a maximum value of ~149 MPa at 10 K. The motion of both the

Pyr-I and -II dislocations is facilitated at higher *T*s (but still below the transition *T*).

3. Under large compression, the Pyr-I edge dislocation transforms into basal-dissociated dislocation core structures over a wide *T* range. The transition of the Pyr-I edge dislocation into the basal-dissociated $\langle c \rangle$ + basal $\langle a \rangle$ structure is enhanced by increasing the compressive strain normal to the slip plane, glide stress, and *T*.

4. All the transformed cores of the Pyr-I $\langle c + a \rangle$ edge dislocations are essentially sessile above the transition *T* because these cores dissociate on the nonglide basal planes. The stress needed to induce a post-transition event is higher than the CRSS for the "tail-cutting" behavior observed below the transition *T*. Thus, the stress for the Pyr-I edge dislocation also exhibits an inverse *T* dependence.

Herein, MD simulations were performed using a relatively high deformation speed compared with experiments and thin simulation models owing to the limitation of calculation costs. A PBC was not applied along the dislocation line, and a thin-film structure was employed to model the Pyr-I slip for enabling dissociation on the basal plane. For a bulk specimen, the presence of three-dimensional constraints may make dissociation more difficult than that predicted based on the current analysis. The Pyr-I and -II $\langle c + a \rangle$ screw dislocations may have completely different dependences on the *T* and nonglide stress than those reported here because the Pyr-I dislocation has been reported to have higher mobilities at lower *T*s.[14,18] The behavior of pyramidal dislocations is quite complex. Further analyses are required to completely understand the slip behavior of these dislocations.

Conflict of Interest

There is no conflict of interest.

Supporting Information

The authors would like to acknowledge financial support from the Japan Science and Technology Agency (JST), CREST (Grant number JPMJCR2094).

References

[1] M. H. Yoo, Slip, twinning, and fracture in hexagonal close-packed metals, *Metallurgical Transactions A*, 1981, **12**, 409-418, doi: 10.1007/BF02648537.

[2] S. R. Agnew, Deformation mechanisms of magnesium alloys, *Advances in Wrought Magnesium Alloys*, Amsterdam: Elsevier, 2012, 63-104, doi: 10.1533/9780857093844.1.63.

[3] M. S. Hasan, R. Lee, W. Xu, Deformation nanomechanics and dislocation quantification at the atomic scale in nanocrystalline magnesium, *Journal of Magnesium and Alloys*, 2020, **8**, 1296-1303, doi: 10.1016/j.jma.2020.08.014.

[4] P.M. Anderson, J.P. Hirth, J. Lothe, Theory of dislocations, 3rd Edition, Cambridge University Press, 2017, **3**, 55-90, doi: 10.1016/0502-8205(53)90018-5

[5] S. Ando, K. Nakamura, K. Takashima, H. Tonda, {1122} <1123> slip in magnesium single crystal, *Journal of Japan Institute of Light Metals*, 1992, **42**, 765-771, doi: 10.2464/jilm.42.765

[6] T. Obara, H. Yoshinga, S. Morozumi, {11$\bar{2}$2} 〈23〉 Slip system in magnesium, *Acta Metallurgica*, 1973, **21**, 845-853, doi: 10.1016/0001-6160(73)90141-7.

[7] J. Zhang, S. P. Joshi, Phenomenological crystal plasticity modeling and detailed micromechanical investigations of pure magnesium, *Journal of the Mechanics and Physics of Solids*, 2012, **60**, 945-972, doi: 10.1016/j.jmps.2012.01.005.

[8] H. Fan, S. Aubry, A. Arsenlis, J. A. El-Awady, Grain size effects on dislocation and twinning mediated plasticity in magnesium, *Scripta Materialia*, 2016, **112**, 50-53, doi: 10.1016/j.scriptamat.2015.09.008.

[9] Haidong, Fan, The role of twinning deformation on the hardening response of polycrystalline magnesium from discrete dislocation dynamics simulations, *Acta Materialia*, 2015, **92**, 126-139, doi: 10.1016/j.actamat.2015.03.039.

[10] Z. Wu, W. A. Curtin, The origins of high hardening and low ductility in magnesium, *Nature*, 2015, **526**, 62-67, doi: 10.1038/nature15364.

[11] H. Fan, Q. Wang, X. Tian, J. A. El-Awady, Temperature effects on the mobility of pyramidal dislocations in magnesium, *Scripta Materialia*, 2017, **127**, 68-71, doi: 10.1016/j.scriptamat.2016.09.002.

[12] B. Devincre, T. Hoc, L. Kubin, Dislocation mean free paths and strain hardening of crystals, *Science*, 2008, **320**, 1745-1748, doi: 10.1126/science.1156101.

[13] N. Bertin, C. N. Tomé, I. J. Beyerlein, M. R. Barnett, L. Capolungo, On the strength of dislocation interactions and their effect on latent hardening in pure Magnesium, *International Journal of Plasticity*, 2014, **62**, 72-92, doi: 10.1016/j.ijplas.2014.06.010.

[14] B. Li, E. Ma, Pyramidal slip in magnesium: Dislocations and stacking fault on the{1011}plane, *Philosophical Magazine*, 2009, **89**, 1223-1235, doi: 10.1080/14786430902936707.

[15] J. F. Stohr, J. P. Poirier, Etude en microscopie electronique du glissement pyramidal{1122} 〈1123〉 dans le magnesium, *Philosophical Magazine*, 1972, **25**, 1313-1329, doi: 10.1080/14786437208223856.

[16] J. Geng, M. F. Chisholm, R. K. Mishra, K. S. Kumar, An electron microscopy study of dislocation structures in Mg single crystals compressed along [0 0 0 1] at room temperature, *Philosophical Magazine*, 2015, **95**, 3910-3932, doi: 10.1080/14786435.2015.1108531.

[17] J. Geng, M. F. Chisholm, R. K. Mishra, K. S. Kumar, The structure of 〈c + a〉 type dislocation loops in magnesium,

Philosophical Magazine Letters, 2014, **94**, 377-386, doi: 10.1080/09500839.2014.916423.
[18] Y. Tang, J.A. El-Awady, Formation and slip of pyramidal dislocations in hexagonal close-packed magnesium single crystals, *Acta Materialia*, 2014, **71**, 319-332, doi: 10.1016/j.actamat.2014.03.022.
[19] H. Fan, J. A. El-Awady, Towards resolving the anonymity of pyramidal slip in magnesium, *Materials Science and Engineering: A*, 2015, **644**, 318-324, doi: 10.1016/j.msea.2015.07.080.
[20] K. Y. Xie, Z. Alam, A. Caffee, K. J. Hemker, Pyramidal I slip in c-axis compressed Mg single crystals, *Scripta Materialia*, 2016, 112, 75-78, doi: 10.1016/j.scriptamat.2015.09.016.
[21] Z. Wu, W. A. Curtin, Intrinsic structural transitions of the pyramidal I <c + a> dislocation in magnesium, *Scripta Materialia*, 2016, **116**, 104-107, doi: 10.1016/j.scriptamat.2016.01.041.
[22] S. Plimpton, Fast parallel algorithms for short-range molecular dynamics, *Journal of Computational Physics*, 1995, **117**, 1-19, doi: 10.1006/jcph.1995.1039.
[23] Z. Wu, M. F. Francis, W. A. Curtin, Magnesium interatomic potential for simulating plasticity and fracture phenomena, *Modelling and Simulation in Materials Science and Engineering*, 2015, **23**, 015004, doi: 10.1088/0965-0393/23/1/015004.
[24] R. Ahmad, Z. Wu, W. A. Curtin, Analysis of double cross-slip of pyramidal I c+a〉 screw dislocations and implications for ductility in Mg alloys, *Acta Materialia*, 2020, **183**, 228-241, doi: 10.1016/j.actamat.2019.10.053.
[25] M. Ghazisaeidi, L. G. Hector Jr, W. A. Curtin, First-principles core structures of edge and screw dislocations in Mg, *Scripta Materialia*, 2014, **75**, 42-45, doi: 10.1016/j.scriptamat.2013.11.013.
[26] S. Sandlöbes, M. Friák, J. Neugebauer, D. Raabe, Basal and non-basal dislocation slip in Mg-Y, *Materials Science and Engineering: A*, 2013, **576**, 61-68, doi: 10.1016/j.msea.2013.03.006.
[27] H. J. C. Berendsen, J. P. M. Postma, W. F. van Gunsteren, A. DiNola, J. R. Haak, Molecular dynamics with coupling to an external bath, *The Journal of Chemical Physics*, 1984, **81**, 3684-3690, doi: 10.1063/1.448118.
[28] A. Stukowski, K. Albe, Extracting dislocations and non-dislocation crystal defects from atomistic simulation data, *Modelling and Simulation in Materials Science and Engineering*, 2010, **18**, 085001, doi: 10.1088/0965-0393/18/8/085001.
[29] J. Dana Honeycutt, H. C. Andersen, Molecular dynamics study of melting and freezing of small Lennard-Jones clusters, *The Journal of Physical Chemistry*, 1987, **91**, 4950-4963, doi: 10.1021/j100303a014.
[30] A. Stukowski, Visualization and analysis of atomistic simulation data with OVITO-the Open Visualization Tool, *Modelling and Simulation in Materials Science and Engineering*, 2010, **18**, 015012, doi: 10.1088/0965-0393/18/1/015012.
[31] Z. Yang, M. F. Chisholm, G. Duscher, X. Ma, S. J. Pennycook, Direct observation of dislocation dissociation and Suzuki segregation in a Mg-Zn-Y alloy by aberration-corrected scanning transmission electron microscopy, *Acta Materialia*, 2013, **61**, 350-359, doi: 10.1016/j.actamat.2012.09.067.